Contents lists available at ScienceDirect

Comptes Rendus Mecanique

Computational methods in welding and additive manufacturing/Simulation numérique des procédés de soudage et de fabrication additive

Process of selective laser sintering of polymer powders: Modeling, simulation, and validation

Aoulaiche Mokrane, M'hamed Boutaous *, Shihe Xin

Université de Lyon, CNRS, INSA Lyon, Université Claude-Bernard Lyon-1, CETHIL UMR 5008, 69621, Villeurbanne cedex, France

A B S T R A C T

Selective laser sintering (SLS) of polymer powders involves multiphysical transient phenomena. A numerical tool for simulating such a process is developed on the basis of the reliable modeling of the corresponding thermo-physical transient phenomena and appropriate numerical methods. The present paper addresses modeling, simulation, and validation aspects that are indispensable for studying and optimizing SLS process. The coupled multiphysical models are detailed, and the numerical tool based on the finite volume method is presented, with validations in terms of numerical and physical accuracy, by considering the shrinkage involved in the process and the successive layers deposition. A parametric analysis is finally proposed in order to test the reliability of the model in terms of representing real physical phenomena and thermal history experienced by the material during the process.

© 2018 Académie des sciences. Published by Elsevier Masson SAS. This is an open access article under the CC BY-NC-ND license (http://creativecommons.org/licenses/by-nc-nd/4.0/).

1. Introduction

The Selective Laser Sintering (SLS) is a promising additive manufacturing technique for modern material processing. It is drawing more and more attention from scientific communities and industries. Although recent technology improvements made it move from rapid prototyping to production, SLS is not yet a reliable process for thermoplastics, because of limited quality of the resultant parts compared to those from classical processes [1].

So that the SLS becomes reliable for thermoplastic materials, more efforts are still needed to understand the physical phenomena involved in the process, model them conveniently, implement the corresponding models in a numerical tool for simulating the different steps of the process, validate the tool and perform relevant studies so as to improve the quality of the final parts. New knowledge and academic developments are therefore needed to perform studies on SLS process and make a link between process, material structure, and parts' final properties.

Despite the apparent simplicity of the SLS concept, the involved physical phenomena are numerous and complex: interaction between laser and powder bed, melting, coalescence of melted grains and air diffusion versus densification, solidification versus crystallization, volume shrinkage, and layers deposition. Furthermore, these phenomena spread over different scales of time and space.

---

* Corresponding author.
  E-mail address: mhamed.boutaous@insa-lyon.fr (M. Boutaous).

Moreover, the quality of SLS parts depends on a large number of process and material parameters: type of polymer, grain size, layer thickness, laser power, diameter of laser beam, scanning velocity, spacing between laser scans, powder spreading speed, preheat temperature, etc.

Considering the melting step, for example, the first modeling necessary to be done concerns how laser beam interacts with powder bed, how the powder melts, how porosity of the powder layer changes and how the thermo-physical properties of the melting zones evolve in time. As evolution of the thermo-physical properties of the melt controls the density and the micro-structure of the final part, faithful models are indispensable. In other words, the corresponding models must be validated.

The models, either validated or not, should be then used in a numerical tool to simulate the whole process. As no commercial software is available, the development of a numerical code is necessary in order to study the SLS of a polymer powder. There arise questions on the approach, the mathematical formulation, and the numerical method to be used. Again, the numerical tool developed needs to be validated before any use for understanding and optimization of the SLS process. This leads to the conclusion that polymers SLS process simulation is a very complex multi-disciplinary work and that tremendous research efforts on the topic are needed to face the challenge. The present paper aims at addressing various needs in the simulation of an SLS process in order to give a global view and presenting some work we realized.

The paper is organized as follows: after detailing the main steps of an SLS process and the modeling aspects of the involved physical phenomena, simulation aspects will be discussed, before presenting the mathematical formulation and numerical methods used and the results obtained in terms of validation; finally, concluding remarks, with discussions of the capabilities of the developed tool, and perspectives for the SLS modeling are given.

2. SLS process and modeling aspects

In an SLS process, both the production and supply zones are preheated to homogenize and reduce the temperature gradient. The preheating temperatures could be different, but they remain slightly below the onset melting point and above the crystallization point [2]. For convenience, it can be considered that both zones are preheated at the same temperature and that preheating does not need to be modeled.

A laser placed above the production zone or the powder bed can be used to merge polymer grains on the surface of the powder bed by means of a scanning mirror. As is mentioned in the introduction, the laser beam interacts with the powder bed, which is a granular material, and the interaction depends on the laser wavelength, the powder distribution size, and the chemical composition of the polymer. The supplied energy in the material is usually represented in the depth direction by an exponential law named Beer–Lambert law, which is also suitable for UV and IR radiation [3]. Many studies simplify the problem and consider only surface interaction [4], but it was widely known and physically proven that it is a volumetric interaction [5,2], involving x-ray diffraction (Mie theory) and the behavior of semi-transparent materials due to the materials' nature [3] and the granular state [6,7]. As the interaction between the laser beam and the polymer powder bed is the starting point of an SLS process, we investigated it in previous works [8,7] by considering absorption, transmission, and diffusion with multiple scattering of the laser beam in a granular material. In fact, most of polymer grains are semi-transparent to laser beam, and their size is close to the laser wavelength. This suggests application of Mie theory. A modified Monte Carlo ray tracing method coupled with Mie theory was then developed and implemented, as in our previous work [7]. The results were validated by a case of both metallic and polymer powders. The application of the method to a polymer powder bed showed important influences of multiple scattering. As observed experimentally, the model predicts a larger heating zone near the bed surface in comparison with the diameter of the laser beam and the heating zone decreases or shrinks with increasing depth [7].

Laser power, provided to polymer grains, heats and melts them. The melted grains coalesce, and this tends to densify the bed and make air between grains escape through open pores to the bed surface. When pores are fully closed, gas diffusion starts, and the densification of the bed continues. Both coalescence and air diffusion induce bed densification and evolution of the bed porosity. They need to be taken into account when modeling the SLS process. There are many works in the literature on coalescence [9,10] and on air diffusion [11,12]. Note that polymer viscosity and surface tension are two important factors for coalescence, but also viscoelasticity and relaxation time (reptation time) play important roles in the densification process compared to metallic materials.

The melting of polymer grains results in an evolution of the powder thermo-physical properties that need to be modeled for accurate simulation of the SLS process. Unfortunately, semi-crystalline polymer grains do not have a fixed melting point: they melt in a range of temperature. In fact, polymers are not pure molecular materials, but are constituted by a statistical distribution of macromolecules, leading to different melting temperatures, as they interact by different Van der Waals forces. During this step, all the evolutions of the thermophysical properties need to be accurately described, and a fusion model is required to link the solid and fully melted states. In terms of energy balance, a heat sink representing latent heat, the amount of energy needed for melting, should appear in the energy equation. As the fusion model proposed by Voller et al. [13] is based on the volume fraction of liquid, we suggest also a similar approach to define the evolutions of the thermo-physical properties during melting.

Another consequence of the bed densification and air exhaust is the volume shrinkage, which should be also considered in simulation of the process. As volume shrinkage is closely related to the evolution of bed porosity, convenient modeling of coalescence and air diffusion is indispensable, and its accuracy is crucial for the predictions of the final part's behavior and
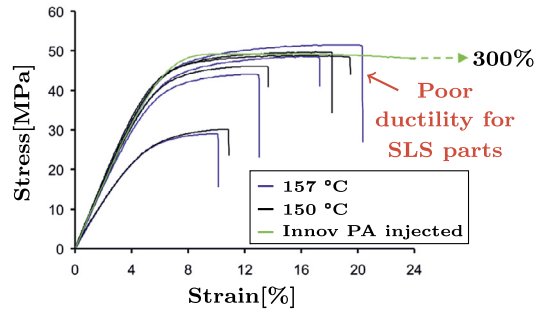
Fig. 1. Stress–strain behavior of a Nylon polymer [1].

quality. In fact, the porosity is responsible of the worst mechanical properties of materials issued from additive manufacturing, compared to classical manufacturing process as shown in Fig. 1. In addition, it is widely established that the ductility of classical materials is higher than that of materials issued from additive manufacturing. The consolidation phenomenon between particles and the remaining porosity in the final part have a great influence on the obtained mechanical properties [14], but also the quality of the welding interfaces between grains plays a great role, which is unavoidable in this process, but not involved in classical ones. After scanning all the paths designed for a given layer, a new one is deposited. A roller is usually used to supply a new powder layer and its spreading speed is smaller than that of laser scanning. Hence, the deposition of a new layer should also be taken into account in the simulation of an SLS process and thus modeled. The laser beam scans the paths designed for this layer: there are again interaction between laser beam and powder bed, melting, coalescence, and air diffusion, as in the first laser-scanned layer, but with new boundary conditions. We should now consider the last layer state and temperature, and thermal interaction between the facing layers, having different physical and thermal histories.

The deposition of new layers is repeated until the whole part is processed. The part will then be cooled down. During this cooling step, crystallization takes place, and another source term appears in the energy equation and corresponds to the exothermal enthalpy generated by the crystallization kinetics. The crystallization process consists in the rearrangement of polymer chains leading to the formation of ordered structures and semi-crystalline regions. The thermophysical properties in these regions depend on the degree of crystallinity and need also to be modeled. As the degree of crystallinity is resulted from crystallization history and conditions, modeling crystallization kinetics is indispensable for simulating an SLS process. The literature about crystallization modeling is rich. The interested reader can find a review with more details in [15–19].

3. Simulation aspects

Apart from the large number of models to be used, there arise several concerns in process simulation of the SLS of a polymer powder: simulating scale, mathematical formulation, numerical methods, and validation.

The powder bed can be considered as a porous or granular medium. Depending on the consideration chosen or simplifying hypothesis, the simulating scale differs. If the polymer powder is viewed as a granular medium, simulation should be done at the grain level. If it is a porous medium, one should adapt the common methodology used to study porous media: the powder bed will be considered as a homogeneous medium, and specific modeling and numerical methods for such materials should be introduced.

In our previous works [8,7], the granular medium of the powder bed was considered. The energy equation was formulated at the grain level and a Discrete Element Method (DEM) was developed to solve the equations. Even if the approach is really interesting, especially to model the laser–powder interaction and to determine the heat source in the process, its computation cost makes its extension to the real part scale difficult.

This led to the consideration of a powder layer as a homogeneous medium. The choice gives rise to some complexity in the mathematical formulation: the thermo-physical properties should be modeled for the equivalent homogeneous medium. It means that another modeling between polymer and air should be added to that on the grain level due to melting and crystallization. Based on the homogenized properties, the energy equation is written and can be solved by the well-known classical numerical methods as finite elements, finite differences or finite volumes. Finite element methods are often used in the literature [20–22,4,23], but there are difficulties to take into account volume shrinkage and deposition of a new layer. As it is easier for finite difference methods or finite volume methods to consider volume shrinkage and deposition of a new layer, we choose finite volume methods to solve the energy equation. Concerning the time scheme, an implicit scheme is chosen in order to use larger time steps and study larger domain sizes and more deposited layers. The last issue of the simulation concerns its validation. In the literature, validation means usually comparison with experimental results with reasonable agreement. In fact, there are three levels of validation: the first one is the validation of various models of the physical phenomena involved in an SLS process, the second one is that of their numerical implementation in a simulation tool, and the last one is that against experimental data. Given the number of models to be used in simulating an SLS process, it would be difficult to get all the models separately validated for a polymer bed, as they interact with each

other, and form a global approach to be validated at the level of the whole process. On the second level, validation works can be done by showing the accuracy of numerical results. Numerical methods and time schemes have their own order of theoretical accuracy. It is important that the simulation tool developed yields numerical results of the same order of accuracy as that suggested by theory. This helps minimizing errors related to numerical implementation of various models and should become the common practice in such approaches developed for simulating the SLS process.

Concerning the last level of validation, there are only few relevant experimental works [5,24,22,2] in the literature, and in all the cases, data inputs for simulations are not completely available. Therefore, needs for experimental works in order to validate the numerical tools are crucial. It constitutes a real need and challenge in studying additive manufacturing processes. It would be interesting to follow a benchmarking approach: a benchmark problem can be commonly defined for a polymer powder with known characteristics, a prescribed SLS process with fixed preheating temperature, a number of laser paths, a number of deposited layers, etc.

4. Mathematical formulation and numerical methods

4.1. Governing equation

The enthalpy of the polymer bed is expressed in terms of temperature and homogenized properties. The physical problem of the SLS process is formulated by the following transient energy balance:

$$\rho C_p \frac{\partial T}{\partial t} = \nabla \cdot (\lambda \nabla T) + Q + S_f + S_c \tag{1}$$

where T is temperature, ρ, C_p, and λ are respectively density, specific heat, and thermal conductivity of the homogenized polymer bed, Q is the volumetric heat source resulted from the interaction between laser beam and polymer bed, S_f is the melting latent heat defined as in [13], and S_c is the crystallization enthalpy provided during the cooling step. Q and S_c are heat sources, while S_f is a heat sink. Note also that Q and S_f can appear at the same time and the same location in the powder bed, and that S_c takes place only after Q and S_f disappear. ρ, C_p, λ, Q, S_f and S_c should all come from modeling.

It is clear that, due to the high viscosity of polymers, all flows could be considered as negligible during modeling, which is not true in the case of metals.

4.2. Modeling the multiphysics phenomena

For the thermo-physical properties of the homogenized powder bed, the effective density and specific heat are calculated using the mixing law that depends on the gas fraction or the porosity φ and on the liquid fraction f_l of the polymer:

$$\rho = (1 - \varphi)\left[(1 - f_l)\rho_{ps} + f_l\rho_{pl}\right] + \varphi\rho_{gas} \tag{2}$$

$$C_p = \left[(1 - \varphi)\left[(1 - f_l)\rho_{ps}(C_p)_{ps} + f_l\rho_{pl}(C_p)_{pl}\right] + \varphi\rho_{gas}(C_p)_{gas}\right]/\rho \tag{3}$$

In the above models, the subscripts 'ps', 'pl', 'gas' indicate, respectively, the solid, liquid, and gas phases. Modeling of thermal conductivity is complicated because it is an intensive quantity, with tensorial representation. There is no general model that allows one to get the effective conductivity of a composite as a function of the different contributions. The thermal conductivity of a powder bed is mainly dictated by the thermal conductivity of the gas present within the voids between grains [25].

For the powder bed, the empirical correlation proposed by Hashin & Shtrikman [26], based on the exact Maxwell model, is used to obtain the effective conductivity of the medium. This model offers the possibility to calibrate the predicted values by the geometric factor d, which is related to the grains' shape:

$$\lambda = \lambda_{gas} \frac{1 + \gamma(d-1)(1-\varphi)}{1 - \gamma(1-\varphi)} \tag{4}$$

$$\gamma = \frac{\lambda_p - \lambda_{gas}}{\lambda_p + (d-1)\lambda_{gas}} \tag{5}$$

Without melting, the λ_p of polymer is equal to λ_{ps}, the thermal conductivity of semi-crystalline polymer. In the case of melting due to the low ratio between the conductivities of the liquid (amorphous) and the semi-crystalline phases, the thermal conductivity of the polymer is calculated using a mixing law proposed by Le Goff et al. [27]:

$$\lambda_p = (1 - f_l)\lambda_{ps} + f_l\lambda_{pl} \tag{6}$$

Note that the parameters ρ, C_p, and λ of the polymer bed depend strongly on the values of f_l and φ that are resulted from melting, coalescence, and air diffusion.

The driving force of an SLS process is the laser source. The spatial distribution of the laser intensity I decays radially as a near-Gaussian function [5]. For a CO_2 laser that is considered here, Defauchy [5] investigated the radial distribution of the beam profile, and proposed a correction of the Gaussian distribution coefficient.
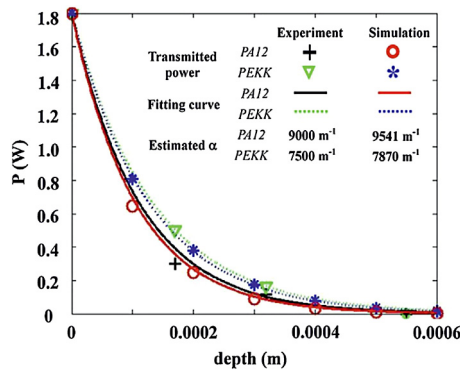
Fig. 2. DEM results versus experimental results of the laser power transmission [7].

To predict the laser beam attenuation through a granular medium, we have developed in our previous work [7] a modified Monte Carlo ray-tracing method, taking into account the absorbed and scattered part of heat flux, using the Mie theory to accurately simulate the power attenuation within a polymer powder bed. A comparison to the experimental investigation done by Peyre et al. [2] is presented in Fig. 2. We showed that the extinction of the laser power in depth direction decreases exponentially following the Beer–Lambert law.

The volumic heat source generated by the laser beam, Q, is given by:

$$Q = (1 - Re)\, I \,\nabla \cdot (e^{-\beta(H-z)}\vec{k}) \tag{7}$$

$$I = \frac{2P}{\pi\, w^2}\, e^{\frac{8\, r^2}{w^2}} \qquad w = \frac{D_1}{1.5}$$

where Re is surface reflectivity of the powder bed, β is the average attenuation coefficient, H is the bed thickness, $\vec{k}$ is the unit vector in the z direction, P is the maximum incident power of the laser, r is the radial distance from the laser axis, and D_1 is the diameter of the laser.

The heat sink in Eq. (1) is related to melting. Voller et al. [13] proposed the following definition:

$$S_f = -(1 - \varphi)\, \delta h\, \frac{\partial f_1}{\partial t} \tag{8}$$

where φ indicates the influence of air which absorbs only sensible enthalpy [28] and δh is the total absorbed latent heat by the polymer as given by Laouadi et al. [29]:

$$\delta h = \rho_{\mathrm{pl}} L + \rho_{\mathrm{pl}} \int\limits_{T_l}^{T} (C_p)_{\mathrm{pl}}\, \mathrm{d}\theta - \rho_{\mathrm{ps}} \int\limits_{T_s}^{T} (C_p)_{\mathrm{ps}}\, \mathrm{d}\theta \tag{9}$$

where L is the latent heat of fusion.

The volumic fractions of the solid and liquid phases satisfy:

$$f_1 + f_s = 1 \tag{10}$$

Given the range of melting temperature $\Delta T = T_1 - T_s$, f_s changes from 1 for $T < T_s$ to 0 at $T = T_1$, while f_1 varies from 0 at $T = T_s$ to 1 for $T > T_1$. A relationship between f_1 and T, $f_1(T)$, is necessary to complete the melting model (8). In the present work, for the sake of simplicity of the numerical phase change treatment as explained by Voller et al. [13], a linear function is introduced:

$$f_1(T) = (T - T_s)/(T_1 - T_s)$$

Above the softening temperature, the particles in contact tend to form interfaces and to decrease their total area by surface forces [30]. Bellehumeur [30], in his work on the analysis of the contact growth between polymer particles, has shown that the viscoelastic character of molten material plays a significant driving role for coalescence, and proposed a modification of Frenkel's model. The modified viscoelastic model, giving the time evolution of the coalescence radius, is used in the present work:

$$8(\Lambda \tau k_1 \frac{\partial \theta}{\partial t})^2 + (2\Lambda \tau k_1 + \frac{\eta\, r_0}{\Gamma}\frac{k_1^2}{k_2})\frac{\partial \theta}{\partial t} - 1 = 0 \tag{11}$$
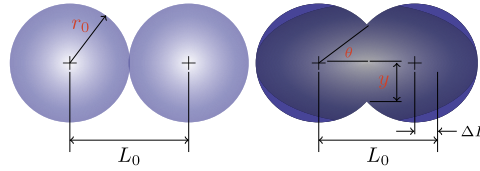
Fig. 3. Schematic of sintering two spherical particles.

$$k_1 = \frac{\sin\theta}{(1+\cos\theta)(2-\cos\theta)} \quad \text{and} \quad k_2 = \frac{2^{-5/3}\cos\theta\sin\theta}{(1+\cos\theta)^{4/3}(2-\cos\theta)^{5/3}}$$

where Λ is the Maxwell model constant (equal to 1 for the upper convected model – UCM – that predicts well the viscoelastic behavior of polymers), θ represents the growth angle between two particles, and τ is the relaxation time of the material. The sintered particles, as in Fig. 3, are assumed to be all spherical and have the same radius r_0 (a mean diameter D_{50} is considered), Γ and η represent the surface tension and the viscosity of the molten polymer. Under certain geometric assumptions, Scherer [31] has linked the neck growth evolution to the relative density, in terms of porosity evolution, leading to:

$$\varphi(t) = 1 - \frac{1-\varphi_0}{\left[1 - \left(\frac{\sin(\theta(t))}{2}\right)^2\right]^3} \tag{12}$$

where φ_0 is the initial porosity and $\varphi(t)$ is the porosity at time t.

With decreasing porosity in time, relative density in the fused region increases and pores can be fully closed. The densification mechanism becomes different. The disappearance of the air bubbles formed inside the polymer will be mainly controlled by the diffusion phenomenon. At this step, the time evolution of the porosity is determined by air diffusion and can be predicted by Mackenzie & Schuttleworth's model [31]:

$$\frac{d\varphi}{dt} = -\frac{3\,\Gamma}{2\,a_0\,\eta}\varphi \tag{13}$$

This equation describes the final stage of densification with relative densities above 0.94. The Mackenzie–Shuttleworth sintering model is based on a closed pore and describes the shrinkage of spherical bubbles in a viscous matrix. The rate of sintering was obtained by the energy dissipated by the viscous flow of the material and the change in the surface area of the pore (a_0 is the initial pore radius).

During the cooling step, the fused polymer crystallizes. The source term of crystallization S_c is then activated in Eq. (1) and can be modeled as follows:

$$S_c = \rho_{ps}\frac{\partial\alpha}{\partial t}\Delta H_c \tag{14}$$

where ΔH_c is the crystallization enthalpy and α is the crystallinity rate.

Crystallization kinetics, time evolution of α, can be obtained by Nakamura's model [23]:

$$\frac{\partial\alpha}{\partial t} = nK(T)(1-\alpha)\left[\ln\left(\frac{1}{1-\alpha}\right)\right]^{\frac{n-1}{n}} \tag{15}$$

where n, the Avrami index, depends on the growth geometry of crystallites and $K(T)$, the anisothermal nucleation rate, is given by Hoffman–Loritzen's theory:

$$K(T) = \ln(2)^{1/n}\cdot K_0\cdot\exp\left(\frac{-U}{R(T-T_\infty)}\right)\cdot\exp\left(\frac{-K_G(T+T_0)}{2T^2\Delta T}\right)$$

with K_0 a constant, U activation energy (6270 J/mol), T_G the glass transition temperature, $T_\infty = T_G - 30$ K, T_0 the thermodynamical fusion point, $\Delta T = T_0 - T$, K_G a constant related to nucleation and R the constant of ideal gases.

All the material parameters are measured, using calorimetric and rheological techniques, as it is usual in our work [15, 16]; details and experimental protocols can be found in [15]. For the material studied in this work, the parameters are taken from [23].

As crystallization concerns only the liquid state, the thermo-physical properties of the fused part evolve during the cooling step, and can be calculated by the following mixing laws:

$$\rho_{pc} = \alpha\rho_{ps} + (1-\alpha)\rho_{pl} \tag{16}$$

$$(C_p)_{pc} = \left[\alpha\rho_{ps}(C_p)_{ps} + (1-\alpha)\rho_{pl}(C_p)_{pl}\right]/\rho_{pc} \tag{17}$$

$$\lambda_{pc} = \alpha\lambda_{ps} + (1-\alpha)\lambda_{pl} \tag{18}$$

To take into account the influence of crystallization on the thermo-physical properties of the polymer bed during the cooling step, it is enough to replace ρ_{pl}, $(C_p)_{pl}$ and λ_{pl} in Eqs. (2), (3), and (6), respectively, by ρ_{pc}, $(C_p)_{pc}$, and λ_{pc}. It is important to note that, during the cooling step f_l in Eqs. (2), (3), and (6) should remain unchanged, and it represents the polymer ratio taking part in crystallization.

4.3. Initial and boundary conditions

Prior to laser scanning, the temperature of the whole powder layer is stated at the initial temperature of the powder T_{ini} and an initial porosity φ_0. The energy equation is subjected to two boundary conditions: at the top surface of the powder bed, the heat exchange by radiation and convection is given as follows:

$$-\lambda\frac{\partial T}{\partial n} = -h_{tot}(T - T_{ext})$$

$$h_{tot} = h + \epsilon\sigma\left(T^2 + T_{ext}^2\right)(T + T_{ext})$$

with T_{ext} is the ambient temperature, h the natural convection coefficient, equal to 15 W·m^{-1}·K^{-1}, ϵ the surface emissivity assumed to be constant and equal to 0.8, σ the Stefan–Boltzman constant.

For the lateral and bottom surfaces, no heat flux exchange is considered. An adiabatic condition is applied:

$$-\lambda\frac{\partial T}{\partial n} = 0$$

n is the normal direction. All the parameter values are detailed further in section 5.2.1.

4.4. Numerical methods

The SLS process involves transient phenomena, and time schemes are necessary to be used in numerical simulations. Accurate description needs appropriate time schemes. Equation (1) is discretized by a semi-implicit second-order Crank–Nicolson scheme:

$$(\rho C_p)^{n+1/2}\frac{T^{n+1} - T^n}{\Delta t} = \nabla\cdot[(\lambda\nabla T)^n + (\lambda\nabla T)^{n+1}]/2 + (Q + S_f + S_c)^{n+1/2} \tag{19}$$

The heating power Q moves in space with a fixed scanning speed and $Q^{n+1/2}$ can be calculated easily. The melting model (8) is discretized in time according to the Crank–Nicolson scheme as follows:

$$S_f^{n+1/2} = (1 - \varphi^{n+1/2})(\delta h)^{n+1/2}\frac{(f_l)^{n+1} - (f_l)^n}{\Delta t} \tag{20}$$

In Eq. (14), the heat source corresponding to crystallization is also discretized in the same way:

$$S_c^{n+1/2} = \rho_{ps}^{n+1/2}\frac{\alpha^{n+1} - \alpha^n}{\Delta t}\Delta H_c^{n+1/2} \tag{21}$$

The coalescence model (11), the air-diffusion model (13), and the Nakamura model (15) are discretized in time by a third-order Runge–Kutta scheme.

Due to the fact that $(\rho C_p)^{n+1/2}$, λ^{n+1}, and $(f_l)^{n+1}$ $(S_f^{n+1/2})$ depend on T^{n+1}, which is the solution to be found, an iterative process is chosen to solve the nonlinear discrete problem in time. We used an accurate updating strategy proposed by Voller et al. [13], although the liquid fraction is considered as linear versus temperature in the range of melting temperatures.

In space, a fixed Cartesian grid is employed for all the quantities and finite volume methods are used to discretize Eq. (19): heat flux on the surfaces of a control volume are discretized by a second-order central-difference scheme. The fully discretized 3D problem is solved using ADI (Alternating Direction Implicit) method: one-dimensional problems in each spatial direction are solved in a successive manner by alternating the spatial directions. As the central-difference scheme results in tri-diagonal matrices in one spatial direction, TDMA (Tri-Diagonal Matrix Algorithm) is used to solve the one-dimensional problems obtained.

With melting of polymer powder, coalescence reduces and removes initial pores, inducing volume shrinkage of the powder bed. Volume shrinkage can be taken into account using special numerical treatments such as two-phase methods or moving mesh technique, which are expensive in computation cost and therefore not feasible for process simulation. In this work, an alternative one-phase approach to achieve volume shrinkage, based on mass conservation, is proposed and presented in Fig. 4. The new volume occupied by the powder bed is inversely proportional to the new density of the molten material. At each time step, the bed volume is updated. An algorithm is used to identify the partly filled cells: shrinked
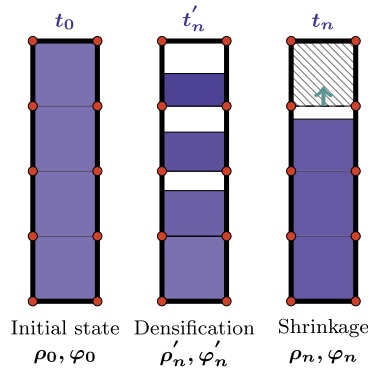
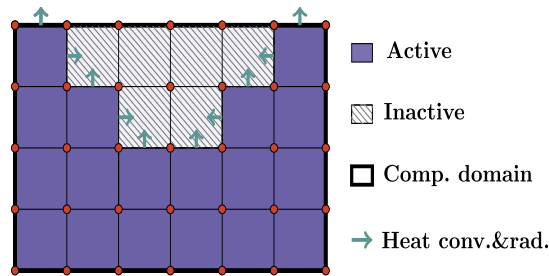**Fig. 4.** Calculation steps of densification.

Fig. 5. Updated bed volume after densification and volume shrinkage.

active cells are displaced to form new active cells to which new physical properties are affected. Surface deformation of the powder bed is followed at each instant and the empty cells will be deactivated as shown in Fig. 5. To avoid complex treatment of non-orthogonal grids, the method that uses the same 3D cubic algorithm to handle curved boundaries proposed in [32] is adopted for calculations. This method can also handle the deposition of a new polymer layer: a bigger grid box is used, and more cells can be activated according to the new layer thickness.

5. Results and validation

5.1. Numerical validation tests

Considering that in our case melting occurs in a range of temperature, there is no analytical solution that can be taken as a reference for comparison with numerical solutions. Hence, to quantify the numerical convergence, the solution error is estimated between the solutions $S_{\Delta h}(x, t)$ and $S_{\frac{\Delta h}{n}}(x, t)$ calculated at a specific time t with time step (or mesh size) Δh and $\frac{\Delta h}{n}$, respectively, by a fixed mesh size (or time step). To quantify the spatial convergence rate, the following norms of error are calculated on the entire domain as follows:

$$\|L\|_1(S_{\Delta h}, S_{\frac{\Delta h}{n}}) = \sum |S_{\Delta h}(x_i, t) - S_{\frac{\Delta h}{n}}(x_i, t)|$$

$$\|L\|_2(S_{\Delta h}, S_{\frac{\Delta h}{n}}) = \sqrt{\sum \left(S_{\Delta h}(x_i, t) - S_{\frac{\Delta h}{n}}(x_i, t)\right)^2}$$

$$\|L\|_\infty(S_{\Delta h}, S_{\frac{\Delta h}{n}}) = \max |S_{\Delta h}(x_i, t) - S_{\frac{\Delta h}{n}}(x_i, t)|$$

Then, the order of convergence in the $\|L\|_j$ norm, P_j is directly estimated by the Richardson extrapolation as follows:

$$P_j = \ln\left[\frac{\|L\|_j\left(S_{\Delta h}, S_{\frac{\Delta h}{n}}\right)}{\|L\|_j\left(S_{\frac{\Delta h}{n}}, S_{\frac{\Delta h}{n^2}}\right)}\right][\ln n]^{-1} \quad, \quad j = 1, \; 2 \text{ and } \infty$$

5.1.1. Spatial convergence rate

Spatial discretization is based on a second-order central-difference scheme, and temperature is localized on the center of a control volume. To avoid interpolation and keep the same grid points to estimate the solution error, one control volume

Table 1

Spatial convergence rate in the case of a simple heat equation.

Grid	$||L||_1$	Order	$||L||_2$	Order	$||L||_\infty$	Order
T						
$25 \times 25 \times 15$	–	–	–	–	–	–
$75 \times 75 \times 45$	1.5276	–	4.5212e–02	–	1.6582e–03	–
$225 \times 225 \times 135$	0.1766	1.96	5.0817e–03	1.99	1.7311e–04	1.99

Table 2

Spatial convergence rate for variables T and f_l in the case of a coupled model.

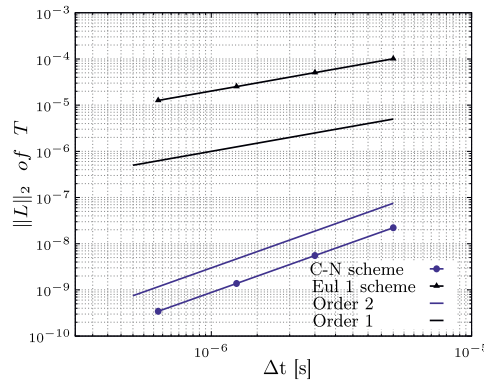| Grid	$||L||_1$	Order	$||L||_2$	Order	$||L||_\infty$	Order
T						
$25 \times 25 \times 15$	–	–	–	–	–	–
$75 \times 75 \times 45$	129.7984	–	4.7261	–	0.6560	–
$225 \times 225 \times 135$	18.2641	1.78	0.7977	1,61	0.1672	1.24
f_l						
$25 \times 25 \times 15$	–	–	–	–	–	–
$75 \times 75 \times 45$	1.1343	–	5.5252e–02	–	6.4958e–03	–
$225 \times 225 \times 135$	0.1365	1.93	6.3376e–03	1.97	7.2947e–04	1.99

Fig. 6. Time convergence rate in the case of a simple heat equation.

is divided into nine in 3D cases (three in each direction): the coarsest grid is common to other finer grids. Two cases are used to show the spatial convergence rate: a heat equation without any source term and a heat equation coupled with a laser source and a melting model (coupled model). The convergence results obtained are summarized in Tables 1 and 2.

As can be seen, in the case of a heat equation without any source terms, the numerical results showed a second-order accuracy, in agreement with theoretical consideration. In the case of the coupled model, the scheme order is sightly reduced for temperature, but the scheme order for the liquid volume fraction remains equal to two. This may be caused by the enthalpic model used because the grid is not suitable for handling the front of fusion, an interface problem. As the liquid volume fraction is around zero near the front, its accuracy is not affected and remains of second order.

5.1.2. Time convergence rate

To show the time convergence rate, computations were performed on a fixed grid of $75 \times 75 \times 45$ cells. Two types of time schemes have been tested: the first-order Euler implicit scheme and the second-order Crank–Nicolson scheme.

In the cases of a simple heat equation and of its coupling with a laser source, Figs. 6 and 7 summarize the results obtained. In both cases, the first-order Euler implicit scheme yielded results of first-order accuracy and the second-order Crank–Nicolson scheme showed a second-order accuracy, which agrees with the theories.

When a heat equation is coupled with both laser source and fusion model, the results obtained in terms of convergence rate for T and f_l are shown in Figs. 8 and 9. The convergence rate for both T and f_l is equal to 1 for both time schemes. Again one observes that the introduction of the fusion model to heat equation, leading to an iterative strategy to deal with latent heat of fusion, affects the second-order accuracy of the Crank–Nicolson scheme. As the difference in computation cost is less than 10% and the semi-implicit scheme is more accurate, the latter is kept for the simulations.

The numerical tests performed to validate the numerical schemes showed that, in most of the cases, the accuracy of the numerical results agrees with theories and that the numerical treatment of the fusion model is not completely satisfactory because the theoretical accuracy of the numerical schemes is reduced from 2 to 1 in time and from 2 to less than 2 in space.
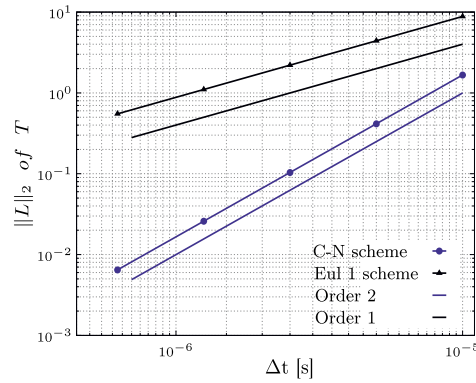
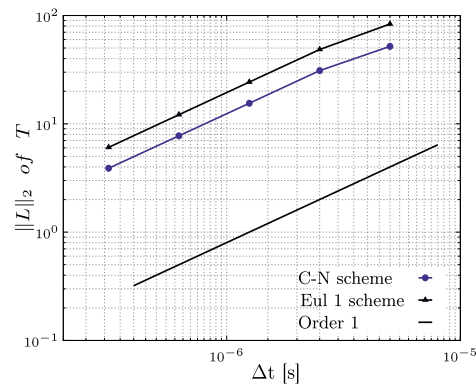**Fig. 7.** Time convergence rate in the case of coupling with a laser source.

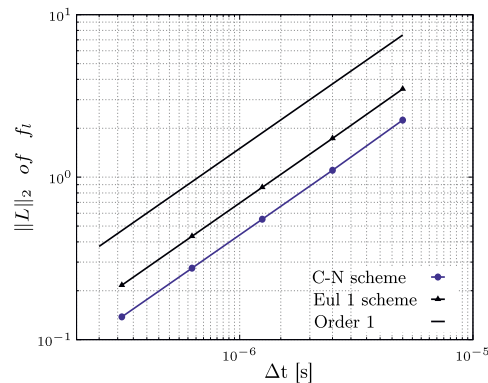**Fig. 8.** Time convergence rate for T in the case of the coupled model.

Fig. 9. Time convergence rate for f_l in the case of the coupled model.

5.2. Experimental validation tests

Once the numerical validation tests of the proposed models have been done, validation tests using experimental results need to be performed to confirm the complete multi-physics 3D modeling. To our knowledge, there is no benchmark available yet to validate the SLS modeling. The work of Riedlbauer et al. [22], concerning a single laser path applied to semi-crystalline polymer powder, seems relevant and is thus taken as the reference of validation. Comparisons concern the temperature distribution and the dimensions of the melted zone.

5.2.1. Material properties and simulation conditions

3D numerical simulations of laser heating of a semi-crystalline polymer PA12 (PA2200) are performed. The simulated volume as shown in Fig. 10 has the dimensions of $3 \times 1 \times 0.5\,\mathrm{mm}^3$; it is fully discretized, with an optimal mesh of
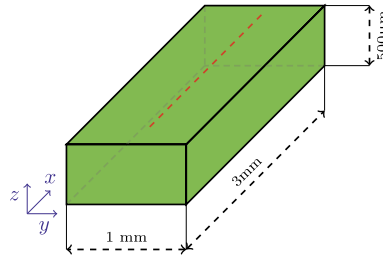
Fig. 10. Simulated specimen geometry.

Table 3
Simulation process parameters.

Case	P [W]	v [ms^{-1}]
1	3.3	0.5
2	3.3	1.0
3	5.6	1.0
4	7.8	1.0
5	7.8	1.5
6	7.8	2.0

Table 4
Powder bed and material properties with process parameters taken from [22],[33], [23], and [5].

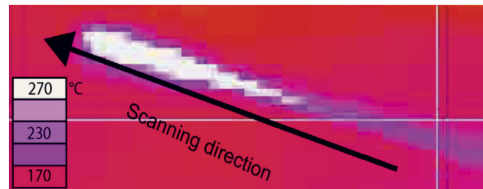| Parameter	Value		Parameter	Value	
ρ_{p_s}	1070	[kg·m^{-3}]	λ_{gas}	0.033	[W·m^{-1}·K^{-1}]
ρ_{p_l}	1022	[kg·m^{-3}]	Cp_{gas}	1049	[J·kg^{-1}·K^{-1}]
Cp_{p_s}	2650	[J·kg^{-1}·K^{-1}]	φ_0	56	[%]
Cp_{p_l}	2650	[J·kg^{-1}·K^{-1}]	D_{50}	60	[µm]
T_s	454	[K]	T_{ini}	445	[K]
T_l	461	[K]	T_{ext}	445	[K]
L	115	[kJ·kg^{-1}]	D_l	400	[µm]
λ_{p_s}	0.28	[W·m^{-1}·K^{-1}]	β	9000	[m^{-1}]
λ_{p_l}	0.24	[W·m^{-1}·K^{-1}]	Re	0.04	[%]

Fig. 11. Infrared camera image of single line laser scanning for case 2 [22].

$150 \times 50 \times 50$ regular cells. Due to the transient nature of the process and the very fast melting kinetics involved by the moving laser source, a time step equal to $5\,^{\mu s}$ was used for all the simulations in order to ensure better convergence and to avoid numerical oscillations.

The initial process conditions needed for calculations were taken from Riedlbauer et al. [22], where laser parameters (scanning velocity **v** and a laser power **P**) for each simulation case are considered. Their values are listed in Table 3.

The powder bed and the thermophysical properties of the material with the process conditions are summarized in Table 4. Therefore, due to the lack of available experimental data, some of the thermophysical properties are assumed to be constant with temperature, and part of them are taken from another type of PA12 and considered as the same for PA2200.

5.2.2. Temperature distribution

The only experimental result available for temperature measurement is the temperature field shown in Fig. 11, which is an infrared camera image of the powder bed's top surface, with laser parameters of case 2. As mentioned by the authors [22], no comparison can be done on the spatial temperature distribution, but only on one focused point.

The simulated temperature distribution at the top surface is presented in Fig. 12, for one laser scan. Due to the low conductivity of the loose powder, the latter does not play any important role in expanding the heated domain, either in width or in depth. The heat-affected zone is delimited by the amount energy of the laser spot and the radiative properties of the powder. The temperature distribution along the laser diameter is controlled by the Gaussian distribution of the laser spot energy, and in depth by the extinction coefficient introduced in the Beer–Lambert law.
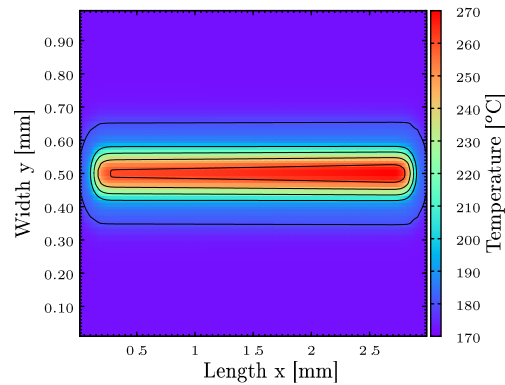
Fig. 12. Temperature distribution at the top surface.

Table 5
Calculated versus experimental melted depth and width.

Case	Fusion depth d_d [μm]			Fusion width d_w [μm]		
	$f_l > 0.99$	$f_l > 0.5$	**Exp**	$f_l > 0.99$	$f_l > 0.5$	**Exp**
1	210	250	138 ∓ 13	320	360	–
2	130	170	109 ∓ 30	200	240	250 ∓ 10
3	190	230	138 ∓ 13	280	320	349 ∓ 36
4	230	270	314 ∓ 20	360	400	–
5	180	220	250 ∓ 12	280	320	–
6	150	190	200 ∓ 14	240	280	–

The maximum temperature measured for this case is 265 °C, and the calculated one is 269.5 °C. The relative error between these values is 4.7% in the range of the heating interval, considering the initial temperature $T_{ini} = 172$ °C.

Moreover, the accuracy of the measurements by the infrared camera depends on the emissivity of the powder bed, and this becomes more pronounced at high temperature. Nevertheless, the simulated temperature results given by the tool we have developed are in good agreement with the measured ones.

5.2.3. Dimensions of the melted zone

The second experimental validation concerns the length and the depth of the melted zone obtained with one laser scan, for different laser parameters (power and scanning speed), taken from the work of Riedlbauer et al. [22], in which experimental data are provided, for the same polymer. In Table 5, we summarized different comparison cases between our simulations and measurements from Riedlbauer et al. [22] with the corresponding histograms in Figs. 14 and 13. A good agreement is clearly obtained, but it depends on how the limits of the melted zone are considered. In Table 5, two limits are presented, by referring to the value of the liquid fraction (f_l), introduced here as a criterion to discriminate the situations. The question is which criterion about the liquid fraction is to be considered to represent the real melted powder particles? Is the melted zone delimited when $f_l = 1$ (completely melted) or less?

In fact, depending on this criterion, the mean relative errors between the simulations and the measurements are in the range of 20% to 25%, for all the six considered cases listed in Table 3.

Franco et al. [24] proposed an experimental analysis of the geometry of the melted zone, for a polyamide powder PA12 as a function of energy density. The measured width and depth of the molten region increase with the energy density and kept localized in the irradiated area by the laser, equivalent to the laser spot's diameter. Qualitatively, the model predictions and the measurements are in real agreement: the calculated widths and depths increase with the energy density, as in the measured cases. The tendencies are also the same in the work of Riedlbauer et al. [22], but the materials are different, and no quantitative comparison is made.

For measured width of the melted zone, we have listed only those for cases 2 and 3 in the referred work. In the other test cases, the authors consider widths larger than the beam spot diameter, except for those cited. In our calculations for these test cases, the computational results are close to the measurements, and never exceed the laser's diameter for all the simulated cases.

The calculated widths and depths when we consider the $f_l > 0,5$ criterion are closer to the measurements in the cases with high laser energy (case 4 and case 5 in Table 3). As the liquid fraction is modeled with a linear function of temperature, and as in the SLS process the temperature is maintained above the melting temperature for a long time, its value increases and expands the molten region. This can explain the quantitative discrepancies observed in this model–experiment comparison.

Furthermore, in the numerical simulation, the laser source has been taken as a continuous energy deposit. In reality, the CO_2 laser works in a pulsed regime. Laser frequency in pulsed regime can give rise to a temperature profile which is
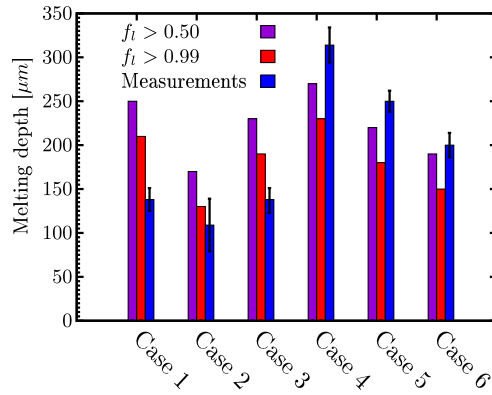
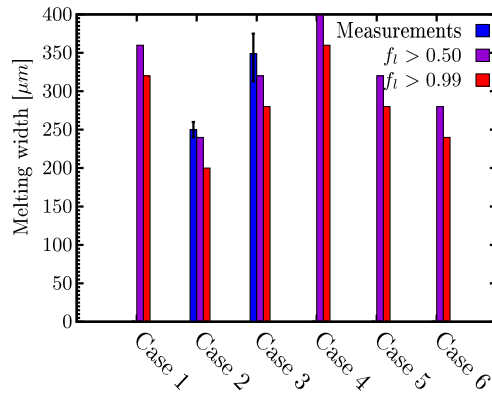**Fig. 13.** Experimental and simulated molten depth results.

Fig. 14. Experimental and simulated molten width results.

different from that in a continuous regime, which has already been highlighted by Peyre et al. [2]. Hence, the choice of laser regime affects also the dimensions of the molten region along the laser path. This could explain partly the discrepancy observed in the comparison.

Conversely, due to the high viscosity and low thermal diffusivity of polymers compared to melted metals, the effect of the volume shrinkage in delimiting the melted zone is not significant. The sintering phenomenon, which is related to the viscosity, takes more time, and the thermal diffusion is lesser compared to radiation, which helps not to extend the melted region.

Note that the real powders are composed of particles with dispersed distribution of size. The diameter of the powder particles ranges between 5 and 100 μm; this affects dramatically the measurement of the melted region as the particles stick on their surface, even when not completely melted in the volume, and hence it can change significantly the results.

5.3. Calculations for five layers

As the SLS process consists in joining layer upon layer, it is interesting to test the developed tool capabilities with the proposed approach in case of simulating the whole SLS process for five powder layers.

For these tests, the geometry is kept the same as in Fig. 10, and the thickness of each layer is 200 μm, with the same energy density as in case 2 ($v = 1.0$ m·s^{-1}, $P = 3.3$ W), but with a laser power equal to 45 W and a scanning velocity of 15 m·s^{-1}. The hatching space between scans is set to 150 μm, which imposes five laser scans by layer.

The analysis will concern quantitatively the involved phenomena, as temperature rising, melting, coalescence, and densification of the material during sintering, the thermal influence of adding new layer upon previously sintered one, and so on. In fact, the thermal history of any point of the part during the process is a key information to predict the final structure and behavior of the part. The temperature distribution at the end of the process allows one to choose the adequate cooling rates and heat treatments for an accurate control of the crystallization kinetics, and hence, the final mechanical behavior. In Fig. 15 is shown the temperature distribution at the top surface during scanning the first layer. During the simulation of the process, once a layer is sintered, for adding a new one, first we proceed with extending the computation domain: the new layer is inactivated numerically by extending the meshed domain progressively, respecting the velocity of the real powder spreading process, equal to 0.2 m·s^{-1}. The mesh cells are activated and followed by moving boundary conditions, which allows us to capture the heat exchange at the interface between the previously sintered layer and the new powder layer,
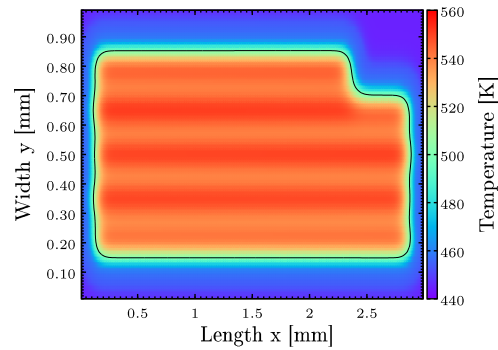
Fig. 15. Top surface temperature distribution while scanning the first layer.
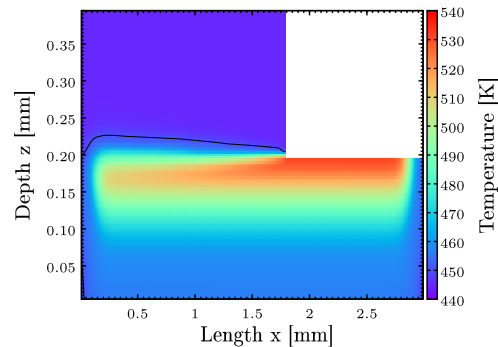

Fig. 16. Temperature in the *ZX* section while adding the second layer.

as illustrated in Fig. 16, representing the temperature distribution in the *ZX* section during the powder deposition of the second layer. Before the second laser scan, the powder spreading is performed along the *x*-axis, and we can see the impact of the powder temperature on the sintered material, where its temperature is cooled down approximatively with 50 K compared to where the powder is not yet deposited (see Fig. 16). In this time, depending on the type of polymer, the processing (or temperature) window is less or more important. The sintered material should be maintained at a temperature between the melting and crystallization values. At high preheating powder temperature, the grains of polymer may stick together and cause processing problems for layer deposition. If the powder is not enough preheated, it can induce the crystallization of the sintered material, causing adhesion problems between the layers. With this capability to highlight this helpful process information, optimization can be done about the preheating temperature and the spreading velocity in order to enhance adhesion at the interfaces between the layers and to propose a protocol for easier processibility of the different polymers. Fig. 17 presents the temperature distribution for five successive sintered layers. Clearly, the material experiences many temperature gradients in both depth and width directions. Many information could be extracted from such simulations. For example, we can observe that the chosen layer thickness (200 μm) is over estimated. A large part of the layer thickness is not heated directly by the laser source. But only the top layer absorbs the power supplied by the laser. The energy is attenuated in the depth, and a part of the last layer is not melted directly by laser interaction, but by thermal diffusion (conduction) from the top newly melted zone and from the lower other already sintered layer. This leads to local thermal kinetics and gradients that differ in the material and hence affect its structure. Nevertheless, an optimal thickness of the layer will help to avoid this kind of problem of belonging regions with poor sintering. The complete thermal history at the interface between the first and second layers is plotted in Fig. 18, representing the temperature evolution during sintering of the five layers. Several steps can be distinguished in the thermal history of the considered point. Firstly, the polymer is melted suddenly when the laser irradiates the material. This step is very fast and depends on the laser parameters (power, scanning velocity, and spot diameter). During the laser traveling on the remaining surface of the part, the considered point cools down due to the top convection and radiation with the ambient temperature. A decrease of the temperature is then observed. After laser scanning of the whole surface, a new layer of powder is supplied. Because of its lower temperature, the interface between these layers is affected, and the temperature decreases by a pure thermal diffusion phenomenon. The thickness and the speed of spreading of the new layer will control the intensity of this thermal exchange. When a new laser scan acts on the top of the added layer, a part of the energy affects the previously sintered layer, and its temperature increases again. The process is repeated until the whole part in sintered. The intensity of this thermal cycling alleviates as the number of supplied layers grows.

After melting, the coalescence and densification phenomena will take place. Of course, with maintaining the melted material at high temperature, viscosity becomes lower and sintering occurs too quickly, yielding less porosity. Fig. 19 shows
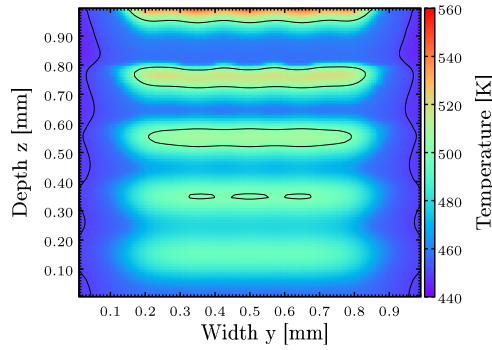
Fig. 17. Temperature distribution in the *ZY* section at the end of the sintering of the last layer.
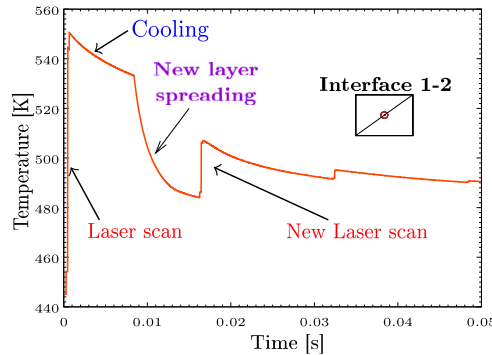

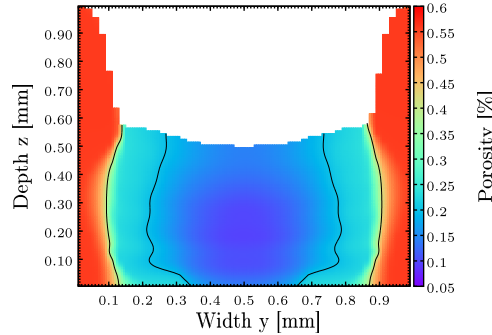**Fig. 18.** Thermal history of the layer interface 1–2 during the process.

Fig. 19. Porosity distribution and densification in the *ZY* section at $t = 2.6$ s.

the porosity distribution and densification. As explained previously, densification causes a volume shrinkage, which depends on the viscosity and the air exhaust kinetics: faster is the sintering kinetics, larger is the shrinkage volume.

Naturally, the central zone of the part is more affected than the borders, which generates more volume shrinkage. At the edges, where the temperature is under the melting value, no sintering occurs. To respect the parts' dimensions, a reduced volume needs to be supplied by the new powder, and tends to make thicker the next layer to be sintered; in consequence, this can lead to worse adhesion between layers. The densification phenomenon due to coalescence and air diffusion induces the reduction of the powder bed's porosity, and hence the thickness of the initial sintered layer, which is directly related to the final dimension of the part.

In terms of SLS process qualification, the mechanical behavior of the final part depends strongly on the remaining porosity at the end of the process. Its prediction with a coupled multiphysics simulation is an effective way for investigating the characteristics of the final part, the geometry and the dimension tolerance versus the process parameters.

For a longer time, once the maximum temperature in the domain is below the melting value, an ambient temperature condition of 298 K is applied to the upper surface for cooling. At this time, below the crystallization temperature, the sintered polymer crystallizes and continue to shrink, its kinetics is described in Eq. (15). In Fig. 20, the crystallization rate in the *zx* section is presented many times after sintering the whole part considered in this study. We can clearly observe an important gradient of crystallization rate in both *z*- and *x*-axes. In the simulation, the laser paths are a succession of round
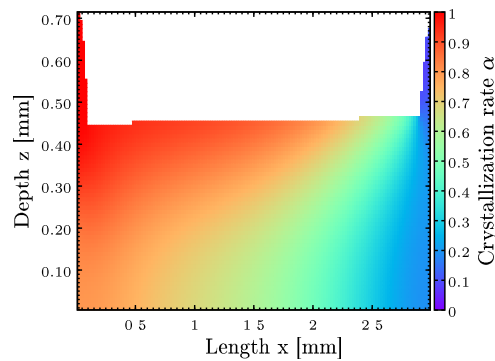
Fig. 20. Crystallization rate in the *ZX* section after 126 s.

trip scans, and the layers are deposited in one direction along the *x*-axis. So this causes a significant temperature gradient that influences the kinetics of crystallization with an important gradient along the *x*-axis. The same phenomenon is observed on the *y*-axis, caused by the scan path strategy. The resulting crystallization gradient is in the diagonal direction of the part, which can induce important residual stresses and warpage in the final part. This analysis highlighted the importance of the several physical coupling involved in the SLS process.

6. Concluding remarks

The present work focused on the global view of simulating an SLS process of polymer powder: various aspects related to modeling, simulation, and validation are discussed in detail.

To be able to study the process, a powder bed is considered as an homogeneous medium for which the governing equations and the multiphysical models of thermo-physical properties, laser power distribution, fusion, coalescence, gas diffusion, and crystallization are formulated.

The governing equations are discretized in time using a second-order semi-implicit Crank–Nicolson scheme and in space using finite-volume methods with second-order scheme. Other time-dependent models are discretized in time using third-order Runge–Kutta methods. Finite-volume methods are chosen because the volume shrinkage due to densification and deposition of a new layer can be considered with ease.

The numerical tool developed was first validated at the numerical level. As the schemes used have their own order of accuracy, the numerical results obtained should show the corresponding order: tests performed for heat equation with laser heating power showed a complete agreement with theories; the results obtained are of second-order both in time and in space; the tests realized with fusion model were less satisfying because the numerical results showed first-order in time and an order higher than one, but less than two in space.

The developed tool was then tested against the experimental study of Riedlbauer et al. [22], which concerned PA12. Depth and width of the melted zone and temperature distribution on the bed surface were used to do the comparison: the results agreed well with the experimental measurements. Furthermore, volume shrinkage due to coalescence and air diffusion and deposition of a new layer were considered, and some results were also presented to show the relevance of the developed tool to analyze the SLS process.

Both validation tests confirmed the quality and pertinence of the proposed modeling, but they also revealed needs for future works: in terms of computation time, it will be necessary to develop simplified models (model reduction) in order to extend this approach for modeling the real industrial part.

An experimental benchmark will be crucial to validate the theoretical models used in simulation because proving their ability to predict the material transformations and thermal histories will constitute an important step in the direction of process understanding and optimization.

References

[1] S. Dupin, Étude fondamentale de la transformation du polyamide 12 par frittage laser : mécanismes physico-chimiques et relations microstructures/propriétés, Ph.D. thesis, INSA de Lyon, 2012.
[2] P. Peyre, Y. Rouchausse, D. Defauchy, G. Régnier, Experimental and numerical analysis of the selective laser sintering (SLS) of PA12 and PEKK semi-crystalline polymers, J. Mater. Process. Technol. 225 (2015) 326–336.
[3] M.F. Modest, Radiative Heat Transfer, Academic Press, 2013.

[4] L. Dong, A. Makradi, S. Ahzi, Y. Remond, Three-dimensional transient finite element analysis of the selective laser sintering process, J. Mater. Process. Technol. 209 (2) (2009) 700–706.

[5] D. Defauchy, Simulation du procédé de fabrication directe de pièces thermoplastiques par fusion laser de poudre, Ph.D. thesis, École nationale supérieure d'arts et métiers – ENSAM, Paris, 2013.

[6] A. Gusarov, I. Smurov, Radiation transfer in metallic powder beds used in laser processing, J. Quant. Spectrosc. Radiat. Transf. 111 (17–18) (2010) 2517–2527.

[7] L. Xin, M. Boutaous, S. Xin, D.A. Siginer, Numerical modeling of the heating phase of the selective laser sintering process, Int. J. Therm. Sci. 120 (2017) 50–62.

[8] L. Xin, M. Boutaous, S. Xin, D.A. Siginer, Multiphysical modeling of the heating phase in the polymer powder bed fusion process, Add. Manuf. 18 (2017) 121–135.

[9] O. Pokluda, C.T. Bellehumeur, J. Vlachopoulos, Modification of Frenkel's model for sintering, AIChE J. 43 (12) (1997) 3253–3256.

[10] M. Kontopoulou, J. Vlachopoulos, Melting and densification of thermoplastic powders, Polym. Eng. Sci. 41 (2) (2001) 155–169.

[11] M. Kontopoulou, J. Vlachopoulos, Bubble dissolution in molten polymers and its role in rotational molding, Polym. Eng. Sci. 39 (7) (1999) 1189–1198.

[12] G. Gogos, Bubble removal in rotational molding, Polym. Eng. Sci. 44 (2) (2004) 388–394.

[13] V. Voller, C. Swaminathan, Eral source-based method for solidification phase change, Numer. Heat Transf., Part B, Fundam. 19 (2) (1991) 175–189.

[14] J.-P. Kruth, G. Levy, F. Klocke, T. Childs, Consolidation phenomena in laser and powder-bed based layered manufacturing, CIRP Ann. 56 (2) (2007) 730–759.

[15] N. Brahmia, Contribution à la modélisation de la cristallisation des polymères sous cisaillement: application à l'injection des polymères semi-cristallins, Ph.D. thesis, INSA de Lyon, France, 2007.

[16] M. Boutaous, N. Brahmia, P. Bourgin, Parametric study of the crystallization kinetics of a semi-crystalline polymer during cooling, C. R. Mecanique 338 (2) (2010) 78–84.

[17] E. Piorkowska, A. Galeski, J.-M. Haudin, Critical assessment of overall crystallization kinetics theories and predictions, Prog. Polym. Sci. 31 (6) (2006) 549–575.

[18] E. Koscher, R. Fulchiron, Influence of shear on polypropylene crystallization: morphology development and kinetics, Polymer 43 (25) (2002) 6931–6942.

[19] I. Coccorullo, R. Pantani, G. Titomanlio, Crystallization kinetics and solidified structure in iPP under high cooling rates, Polymer 44 (1) (2003) 307–318.

[20] J.C. Nelson, S. Xue, J.W. Barlow, J.J. Beaman, H.L. Marcus, D.L. Bourell, Model of the selective laser sintering of bisphenol-A polycarbonate, Ind. Eng. Chem. Res. 32 (10) (1993) 2305–2317.

[21] G. Bugeda Miguel Cervera, G. Lombera, Numerical prediction of temperature and density distributions in selective laser sintering processes, Rapid Prototyping J. 5 (1) (1999) 21–26.

[22] D. Riedlbauer, M. Drexler, D. Drummer, P. Steinmann, J. Mergheim, Modelling, simulation and experimental validation of heat transfer in selective laser melting of the polymeric material PA12, Comput. Mater. Sci. 93 (2014) 239–248.

[23] A. Amado, M. Schmid, K. Wegener, Simulation of Warpage Induced by Non-Isothermal Crystallization of Co-Polypropylene During the SLS Process, AIP Conference Proceedings, vol. 1664, 2015, 160002.

[24] A. Franco, L. Romoli, Characterization of laser energy consumption in sintering of polymer based powders, J. Mater. Process. Technol. 212 (4) (2012) 917–926.

[25] E. Tsotsas, H. Martin, Thermal conductivity of packed beds: a review, Chem. Eng. Process. Process Intensif. 22 (1) (1987) 19–37.

[26] Z. Hashin, S. Shtrikman, J. Appl. Phys. 33 (10) (1962) 3125–3131.

[27] R. Le Goff, G. Poutot, D. Delaunay, R. Fulchiron, E. Koscher, Study and modeling of heat transfer during the solidification of semi-crystalline polymers, Int. J. Heat Mass Transf. 48 (25) (2005) 5417–5430.

[28] K. Nayak, S. Saha, K. Srinivasan, P. Dutta, A numerical model for heat sinks with phase change materials and thermal conductivity enhancers, Int. J. Heat Mass Transf. 49 (11) (2006) 1833–1844.

[29] A. Laouadi, M. Lacroix, N. Galanis, A numerical method for the treatment of discontinuous thermal conductivity in phase change problems, Int. J. Numer. Methods Heat Fluid Flow 8 (3) (1998) 265–287.

[30] C.T. Bellehumeur, M. Kontopoulou, J. Vlachopoulos, The role of viscoelasticity in polymer sintering, Rheol. Acta 37 (3) (1998) 270–278.

[31] G.W. Scherer, Viscous sintering of a bimodal pore-size distribution, J. Am. Ceram. Soc. 67 (11) (1984) 709–715.

[32] J.C. Chai, H.S. Lee, S.V. Patankar, Treatment of irregular geometries using a Cartesian coordinates finite-volume radiation heat transfer procedure, Numer. Heat Transf. 26 (2) (1994) 225–235.

[33] L. Verbelen, S. Dadbakhsh, M. Van den Eynde, J.-P. Kruth, B. Goderis, P. Van Puyvelde, Characterization of polyamide powders for determination of laser sintering processability, Eur. Polym. J. 75 (2016) 163–174.